AIAA JOURNAL
Vol. 46, No. 10, October 2008

Active Flow Control at Low Angles of Attack: Stingray Unmanned Aerial Vehicle

John A. N. Farnsworth,* John C. Vaccaro,* and Michael Amitay†
Rensselaer Polytechnic Institute, Troy, New York 12180

DOI: 10.2514/1.35860

Active flow control using fluidic actuators, via arrays of synthetic jet actuators, was used to provide control power for the Stingray unmanned aerial vehicle in the longitudinal (pitch) and lateral (roll) directions at low angles of attack. Using this technique, the pitch and roll moments were altered such that the effect is similar to that of a deflection of conventional control effectors. The control effectiveness of the synthetic jets on the aerodynamic performance of the Stingray unmanned aerial vehicle was investigated experimentally in a wind tunnel. Global flow measurements were conducted, where the moments and forces on the vehicle were measured using a six-component sting balance. The effect of the actuation was also examined on the surface static pressure at two spanwise locations. In addition, a particle image velocimetry technique was used to quantify the flowfield over the model, both the global flowfield as well as the localized interaction domain near the synthetic jet orifice. The synthetic jets were able to alter the local streamlines and displace the boundary layer through the formation of a small quasi-steady interaction region on the suction surface of the Stingray unmanned aerial vehicle's wing. Phase-locked particle image velocimetry data were acquired to provide insight into the growth, propagation, and decay of the synthetic jets impulse and their interaction with the crossflow. Furthermore, the changes induced on the moments and forces can be proportionally controlled by either changing the momentum coefficient or by driving the synthetic jets with a pulse modulation waveform. This can lead the way for future development of closed-loop control models.

Nomenclature

A_w = wing area
b = span
b_{local} = local span
C_D = drag coefficient
C_L = lift coefficient
C_{Lb} = lift coefficient for the baseline wing
C_{Lf} = lift coefficient with flow control
C_m = pitching moment coefficient about the moment reference center
C_{mb} = pitching moment coefficient for baseline wing about the moment reference center
C_{mf} = pitching moment coefficient with flow control about the moment reference center
C_P = pressure coefficient
C_ℓ = rolling moment coefficient
$C_{\ell b}$ = rolling moment coefficient for baseline wing
$C_{\ell f}$ = rolling moment coefficient with flow control
C_μ = synthetic jets momentum coefficient
$\bar{c}$ = mean aerodynamic chord
c_{local} = local chord length
c_r = root chord
F^+ = reduced frequency
f_c = synthetic jets carrier frequency
f_{mod} = synthetic jets modulation frequency
h_j = width of the synthetic jet slit
$\bar{I}_j$ = time-averaged synthetic jet momentum
l_j = length of the synthetic jet slit
n = number of active synthetic jets
Re_{U_∞} = aerodynamic chord Reynolds number
t_{TOF} = time of flight, $t_{\text{TOF}} = U_\infty / c_{\text{local}}$
U_∞ = freestream velocity
u_j = phase-averaged synthetic jet centerline velocity
X_{MRC} = moment reference center location from nose
x = coordinate in the streamwise direction
x_j = coordinate in the streamwise direction from the synthetic jet orifice
y = coordinate along the wing span
z_j = coordinate in the vertical direction from the synthetic jet orifice
α = angle of attack, degrees
ΔC_L = lift control power, $C_{\text{Lf}}–C_{\text{Lb}}$
ΔC_m = pitching control power, $C_{\text{mf}}–C_{\text{mb}}$
ΔC_ℓ = rolling control power, $C_{\ell f}–C_{\ell b}$
ΔZ_j = normal distance between consecutive velocity vectors
δ = boundary-layer thickness
Λ_{LE} = leading-edge sweep angle, degrees
ν = kinematic viscosity
ρ = air density
τ = synthetic jet outstroke time, $\tau = T/2$
ϕ = phase along the synthetic jet cycle
Ω_y = y component of the vorticity, $\Omega_y = (\partial w / \partial x) - (\partial u / \partial z)$

I. Introduction

RESEARCH on flow control has been one of the major topics in fluid mechanics in the past couple of decades. Most flow control techniques have been focused on control of separation, which has been achieved by either passive or active techniques. The active flow control techniques typically exploit the combined narrowband receptivity of the separating shear layer and the upstream boundary layer to external actuation (e.g., Ho and Huerre [1]). Oster and Wygnanski [2] and Roberts [3] showed that the actuation can affect the global flowfield by modifying the evolution and interactions of the large-scale vortical structures. These modifications can lead to a Coanda-like deflection of the separating shear layer toward the surface (e.g., Seifert et al. [4]) such that the layer vortices are advected downstream in close proximity to the surface.

Presented as Paper 4426 at the 25th AIAA Applied Aerodynamics Conference, Miami, FL, 25–28 June 2007; received 26 November 2007; revision received 15 May 2008; accepted for publication 24 May 2008.

*Graduate Student, Mechanical Aerospace and Nuclear Engineering, 110 8th Street.

†Assistant Professor, Mechanical Aerospace and Nuclear Engineering, 110 8th Street, Corresponding Author; amitam@rpi.edu. Senior Member AIAA.

The approach of virtual modification of the surface may also be applied at low angles of attack, as was shown by Chatlynne et al. [5] and Amitay et al. [6] on a 2-D Clark-Y airfoil. This approach makes it more attractive for the majority of aircraft, which do not fly near separation conditions. When fluidic modification to a baseline is used, the airfoil shape is virtually altered, which can have significant implications for vehicle flight control using flow control. Thus, it might be possible to replace the conventional control surfaces (e.g., flaps, ailerons, rudder, etc.) with active flow control. This is one of the goals of the present paper.

Over the past couple of decades, flow control over finite wings has focused on controlling the flow over delta wings at high angles of attack, where the flow separates from the leading edges and forms shear layers that roll up into two large vortices. As the angle of attack further increases, the leading-edge vortices break down; this can result in wing stall and induce vibrations and buffeting (Sheta et al. [7]). Control of these types of flows has been achieved by using either steady or unsteady means. The steady techniques include leading-edge slats, spanwise blowing, tangential blowing, trailing-edge blowing, and along-core blowing (e.g., Mitchell and Delery [8]). Recently, Gutmark and Guillot [9] used along-core blowing on a highly swept delta wing, which incorporated a jet directed down the vortex core and showed a delay of the vortex breakdown. The unsteady techniques include unsteady blowing, synthetic jets (e.g., Margalit et al. [10]), and oscillating leading-edge microelectromechanical system fabricated flaps (Huang et al. [11]). Although a lot of work has been done on finite wings, it has focused on high angles of attack.

Fluidic surface modification opens up a broad range of alternative flow control methodologies. Amitay et al. [6] showed that the combination of a solid obstruction with a synthetic jet actuator on a 2-D airfoil resulted in the formation of a quasi-steady recirculating region, where its streamwise and cross-stream extent depends on the actuation frequency and the momentum coefficient of the synthetic jet. They showed that, as the actuation frequency increases, the size of the circulation region decreases. In the present paper, we present a technique for 3-D configurations, focusing solely on the ability of arrays of synthetic jets to create similar quasi-steady regions near the surface of the wing.

Such control capability has important applications, not only for external flows but also in a number of internal flows (e.g., between blades of successive stages in turbomachinery, flow in short serpentine inlets, etc.). An important attribute of active modification of the apparent shape of aerodynamic surfaces is that it can enable a new approach to aerodynamic design and emphasize the utility of this approach in lieu of conventional control surfaces, thus saving weight and improving vehicles' overall performance *throughout their flight envelope*.

Almost all the existing active flow control techniques fail to induce meaningful effects when the flow is fully attached (i.e., low angles of attack). The concept proposed by Chatlynne et al. [5] and Amitay et al. [6] of modifying the apparent aerodynamic shape of aerosurfaces to prescribe the streamwise pressure distribution, and therefore to influence its aerodynamic performance, is not new and was addressed in a substantial body of work in the 1940s and 1950s. One example of this approach is the use of a stationary, trapped vortex to alter the apparent local surface curvature and therefore the direction of the external flow (Perkins and Hazen [12]). They used a suction slot near the trailing edge of an airfoil and an upstream cavity to trap a vortex near the trailing edge, and reported substantial lift ($C_L = 1.2$) at zero angle of attack at relatively low (3%) suction coefficient. Mandl [13] used a split flap located on the pressure side of an airfoil combined with suction (at the flap) to trap a vortex and to enforce tangential flow near the trailing edges of the airfoil and the flap and alter the Kutta condition of the airfoil.

In the present work, we experimentally explore the feasibility of using fluidic control (via synthetic jet actuators) on the Stingray unmanned aerial vehicle (UAV) at low angles of attack. This is accomplished by the formation of a small quasi-steady flow interaction domain adjacent to the surface that displaces the local streamlines sufficiently to modify the local pressure distribution. Here, the interaction domain is formed on the upper (suction) surface of the Stingray wing (near the leading edge) by activating arrays of synthetic jet actuators.

Recent work by Amitay et al. [14,15], Parekh et al. [16], and Washburn and Amitay [17] showed very promising results of the integration of active flow control (via leading-edge synthetic jet actuators) in flight control of the Stingray UAV. In these experiments, synthetic jet actuators were mounted along the leading edges and were driven with a pulse modulation waveform, where the effects of the modulation frequency, duty cycle, and the momentum coefficient on the moments and forces were investigated at moderate-to-high angles of attack. The most striking result from that work was that active flow control via leading-edge zero-net-mass-flux-jets was able to affect significant control moments on the vehicle *even when compared with conventional flaps*. For example, at moderate-to-high angles of attack, flow control yielded similar or even larger roll moments than the ailerons (deflected at up to 15 deg). Furthermore, using synthetic jets, *in addition to the flaps*, results in an even larger roll moment. Another striking result was that the direction of the roll can be changed merely by adjusting the modulation frequency.

These effects are related to the interaction mechanism of the arrays of the synthetic jets with the 3-D flowfield, which is more complex than the "virtual aeroshaping" on 2-D airfoils described by Amitay et al. [6] and Chen and Beeler [18]. From pressure data, it was evident that different modulation frequencies result in different "virtual" modification of the shape, which varies at different locations on the wing. However, for a low aspect ratio wing (i.e., the Stingray), the vorticity cannot be accumulated in a manner similar to 2-D airfoils due to the continuous advection and shedding of vorticity near the leading edges.

The major objective of the present paper is to expand the application of the virtual surface modification technique to the Stingray at low angles of attack, where "conventional" flow control techniques have very limited (to no) effect. This could enable the vehicle to be controlled without any moving (external) parts, which can be applied in stealth vehicles during cruise. The motivation here is to use synthetic-jet-based active flow control for longitudinal (pitch) and lateral (roll) control of the Stingray UAV during cruise flight (i.e., at low angles of attack) instead of conventional control surfaces, and thus improve its stealth capabilities. Note that other benefits of using synthetic jets are their simplicity, light weight, and cost, as discussed by Amitay et al. [15] on a full-scale model of the Stingray UAV.

II. Experimental Setup

The experiments were conducted in a closed-return low-speed wind tunnel at Rensselaer Polytechnic Institute having a square cross section of 60 cm, with a maximum speed of 100 m/s, and a turbulence level of less than 0.25%. The wind tunnel is equipped with a six-component sting balance, a dedicated hot-wire anemometry system, a 32 channel pressure scanner, and a particle image velocimetry (PIV) system.

In the present experiments, a 12.5% scale model of the Stingray UAV was designed and fabricated using stereolithography. The model has a root chord of 22 cm, a span of 30 cm, and was designed to incorporate different configurations of elevons at varying degrees to obtain the vehicle's conventional control authority. Figure 1 presents the model with an assortment of elevons that were tested. Note that, for the experiments where active flow control was used, a 14% scale model of the Stingray UAV was designed and fabricated. The 14% scale model has a root chord of 25 cm, a span of 38 cm, a leading-edge sweep angle of 50 deg, and the moment reference center is located 11 cm from the nose. The model incorporates 41 static pressure ports on the starboard wing (and nine on the port wing for symmetry evaluation), which are located in two pairs of two arrays (one parallel to the flow direction, one perpendicular to the leading edge of the wing) at $y/b = 0.33$ and 0.66. In the present experiments, pressure data were acquired only at the ports parallel to the flow direction. The model also has the ability to incorporate four hot film shear stress sensors to detect flow separation; however, because the

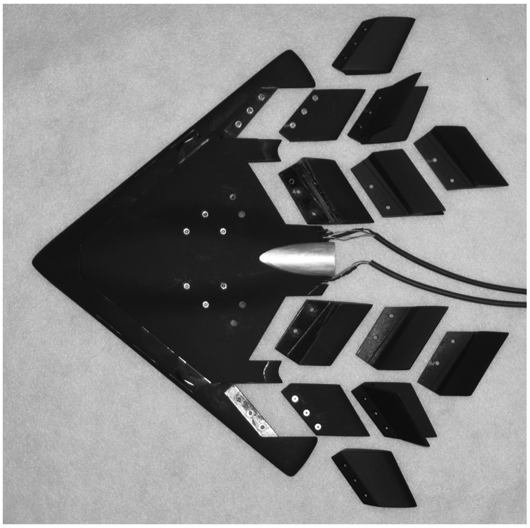

Fig. 1 Stingray wind-tunnel model instrumented with multiple configurations of conventional elevons.

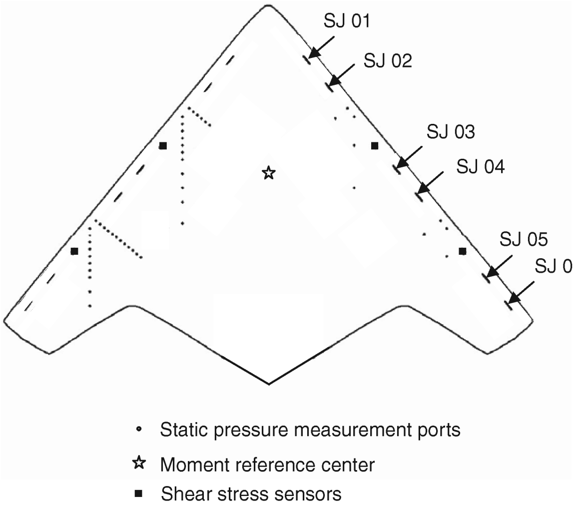

Fig. 2 Stingray wind-tunnel model upper surface geometry with the locations of the static pressure ports, shear stress sensors, and synthetic jet actuators slots.

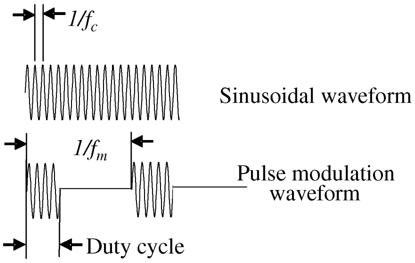

Fig. 4 Comparison of sinusoidal waveform to a pulse modulation waveform.

present work focused on low angles of attack, they were not used in the data presented here.

The pressure scanner, used to measure the static pressure distribution, incorporates a combination of channels with a maximum range of each ±1 psid (pounds per square inch differential) and ±10 in. of water column (±0.36 psid), with an approximate error of ±0.05% of full scale, which corresponds to errors in the reading of $\pm 1.8 \times 10^{-4}$ psid and $\pm 5 \times 10^{-4}$ psid, respectively. Likewise, the six-component sting balance had maximum ranges of ±50 lb for each lift, drag, and side force, ±75 in · lb for each pitch and yaw moment, and ±25 in · lb for roll moment, and with an approximate error of ±0.15%, corresponding to ±0.075 lb, ±0.1125 in · lb, and 0.0375 in · lb, respectively.

The model incorporates 12 pairs of synthetic jets (six on each wing) that are issued through rectangular orifices, each having a width of 0.5 mm and a length of 8 mm. The synthetic jets are located 10 mm from the leading edge. Figure 2 shows the pressure port locations, the synthetic jet slots, and shear stress sensor locations on the top surface of the model, whereas Fig. 3 shows a photo of the Stingray wind-tunnel model with the bottom cover removed for viewing the internal instrumentation. The synthetic jets are formed by the periodic motion of a 20-mm-diam piezoelectric disk mounted on the bottom wall of a sealed cavity. (The formation and evolution of synthetic jets is described, in detail, in the work by Glezer and Amitay [19], Amitay and Cannelle [20], and Cannelle and Amitay [21].)

In the present experiments, the synthetic jets are driven at a carrier frequency of $f_c = 1900$ Hz, where the characteristic frequency of the flow over the Stingray model is $\mathcal{O}(200\ \text{Hz})$, based on the freestream and the mean chord. Thus, the actuation frequency is at least an order of magnitude higher, which results in a quasi-steady virtual shape modification (as will be shown later). Furthermore, this enables the use of different actuation waveforms, as shown in Fig. 4 and described by Amitay and Glezer [22]. Three modulation frequencies were tested: 380, 190, and 95 Hz, each of which was tested at two duty cycles. The first duty cycle was 25% of the modulation period and the second duty cycle was coupled with the

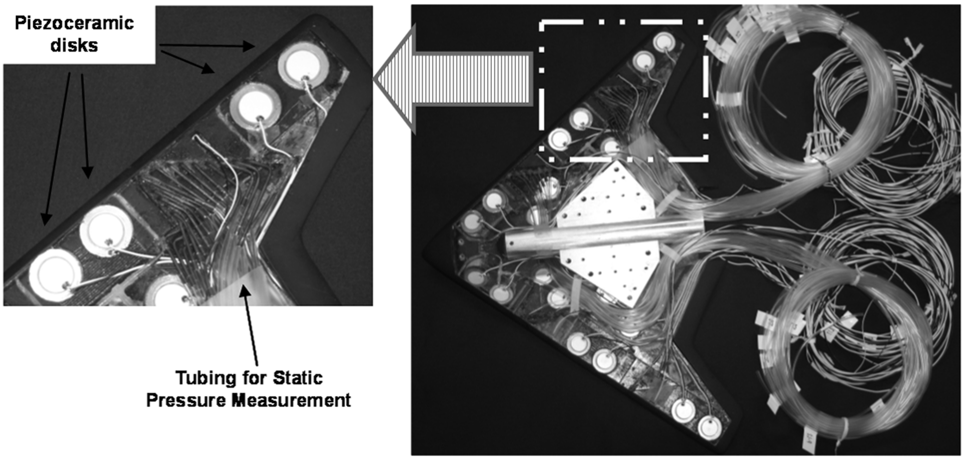

Fig. 3 Stingray wind-tunnel model with bottom cover removed for viewing of the internal instrumentation.

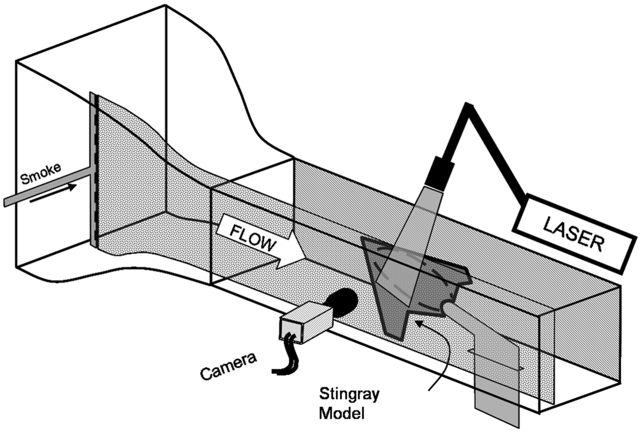

Fig. 5 Wind-tunnel integrated PIV system layout.

modulation frequency to obtain one cycle of the carrier frequency per modulation period, yielding a duty cycle of 20, 10, and 5%, respectively.

In the present work, the freestream velocity was kept constant at 30.5 m/s for the 12.5% scale model and 25 m/s for the 14% scale model, resulting in a mean aerodynamic chord Reynolds number of $Re_{U_\infty} = 185,000$. The Reynolds number is defined as

$$Re_{U_\infty} = \frac{U_\infty \bar{c}}{\nu} \tag{1}$$

where U_∞ is the freestream velocity, $\bar{c}$ is the mean aerodynamic chord of the wing, and ν is the kinematic viscosity.

The strength of the synthetic jets relative to the freestream is quantified by the momentum coefficient C_μ, defined as

$$C_\mu = \frac{n\bar{I}_j}{(1/2)\rho U_\infty^2 A_w} \tag{2}$$

where U_∞ is the freestream velocity, A_w is the wing area, ρ is the density of air, n is the number of active synthetic jets, and $\bar{I}_j$ is the time-average synthetic jet momentum during the outstroke, defined as

$$\bar{I}_j = \frac{1}{\tau}\rho l_j h_j \int_0^\tau u_j^2(t)\,\mathrm{d}t \tag{3}$$

where τ is the synthetic jet outstroke time (one-half of the actuation time period), l_j and h_j are the length and width of the synthetic jet slit, respectively, and $u_j(t)$ is the phase-averaged centerline velocity at the synthetic jet exit plane (measured using a single hot-wire sensor). For the experiments presented in this paper, the momentum coefficient range was $6.25 \times 10^{-5} < C_\mu < 1 \times 10^{-3}$.

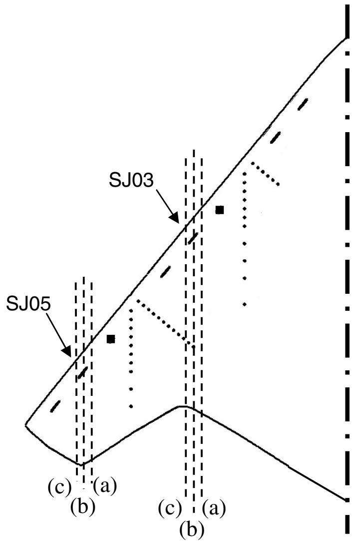

Fig. 6 PIV measurement planes on the top surface of the Stingray wind-tunnel model. Dashed lines are measurement planes.

The interaction of the synthetic jets with the cross stream was captured and investigated through the use of PIV. Two-dimensional velocity vector fields, in the streamwise direction, were collected above the surface of the Stingray model, focusing on the location near the leading edge to explore the interaction between the synthetic jets and the crossflow. The PIV system used is a commercial LaVision System of hardware and software, including two 120 mJ Nd:YAG lasers and a 1376 × 1040 pixel resolution thermoelectrically cooled 12-bit charge-coupled device (CCD) camera. Cylindrical lenses of 50 or 20 mm (for the zoomed-in or zoomed-out measurements, respectively) were used to create the light sheet and a focal lens (with a focal length range of 500–1500 mm) was used to focus the sheet at the measurement domain (the thickness of the light sheet at the center of the measurement domain was about 1 mm). The laser light sheet was then aligned with the area of interest using a computer-controlled three-axis traversing system mounted on the ceiling of the test section. Flow was seeded with $\mathcal{O}(1\ \mu\mathrm{m})$ smoke particles, generated by a theatrical fog machine, in the form of a vertical sheet injected into the freestream flow in the settling chamber of the wind tunnel (Fig. 5). The flowfield was imaged using the CCD camera mounted on its own independently controlled three-axis traverse. Measurements were acquired at six spanwise planes on the Stingray model, focusing on the centerlines of synthetic jet numbers 3 and 5 (SJ03 and SJ05, respectively) on the starboard wing of the model and 5 mm to either side of centerline planes (Fig. 6).

The streamwise velocity components (U, V) were computed from the cross-correlation of pairs of successive images with 50% overlap between the interrogation domains. The images were processed

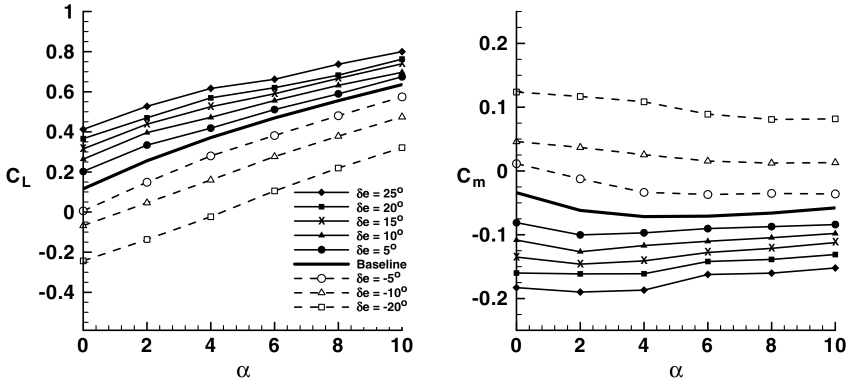

a) b)

Fig. 7 Baseline vehicle forces and moments with conventional elevon deflections vs α: a) lift coefficient and b) pitching moment coefficient.

using an advanced multipass method where the initial and final correlation passes were 64×64 pixels and 16×16 pixels, respectively. Five hundred image pairs were acquired for both the time-averaged and phase-averaged measurements. The camera was mounted at a perpendicular distance of approximately 1 m to the laser light, such that the distance between pixels is from 20 to 106 μm for the zoomed-in and zoomed-out measurements, respectively. The maximum velocity (25 m/s) corresponds to an average displacement of approximately 8 pixels with an approximate error of ± 0.1 pixels, which corresponds to a maximum error of $\pm 1.25\%$ of the freestream velocity (± 0.5 m/s).

III. Results and Discussion

Synthetic-jet-based flow control on the Stingray UAV has been previously investigated thoroughly at moderate-to-high angles of attack by Amitay et al. [14,15], Parekh et al. [16], and Washburn and Amitay [17]. However, aircraft do not normally operate under these conditions, opening the question on the effectiveness of synthetic jet control at low angles of attack. In the following discussion, the effect of flow control, via arrays of synthetic jet actuators, was explored in wind-tunnel measurements on the Stingray model at low angles of attack. The aerodynamic characteristics of the baseline Stingray with conventional effectors are presented in Sec. III.A, followed by the effects (on the aerodynamic characteristics) produced by the synthetic jet actuators in Sec. III.B. The aerodynamic characteristics of the model were analyzed through the use of a six-component sting balance and surface pressure measurements at two spanwise locations ($y/b = 0.33$ and 0.66). Finally, these effects were further investigated in Sec. III.C through PIV measurements that were acquired globally, across the full wing chord, as well as locally, at a location near the leading edge (to explore the interaction domain) at two spanwise locations ($y/b = 0.48$ and 0.82).

A. Baseline Aerodynamics

Before examining the effect of synthetic-jet-based flow control on the aerodynamic performance of the Stingray UAV, the control effectiveness of the conventional effectors was evaluated. The aerodynamic coefficients of the baseline Stingray (i.e., no synthetic jets) and the control power of the effectors were measured using a six-component sting balance, and are presented in Fig. 7. The change of the lift coefficient with angle of attack is presented in Fig. 7a, whereas the pitching moment is displayed in Fig. 7b, each at different elevon deflection angles. Without elevon deflection, the lift coefficient increases linearly with angle of attack for $\alpha < 7$ deg (Fig. 7a), whereas, for larger angles of attack, the increase of the lift coefficient is more gradual. As expected, when the elevons are deflected down (positive δ_e) or up (negative δ_e) symmetrically, the lift is increased and decreased, respectively, with respect to the baseline case (i.e., no elevon deflection).

In addition to the forces, the moments were also measured and the pitching moment (about the moment reference center) is shown in Fig. 7b. Without elevon deflection, the pitching moment has a

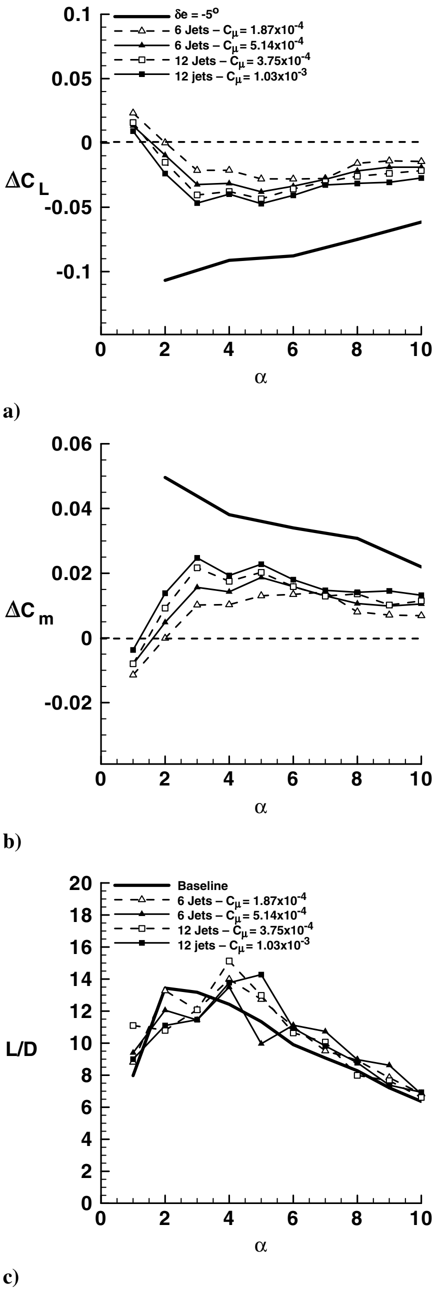

Fig. 8 Synthetic jets are activated with sinusoidal waveform at several momentum coefficients: a) lift control power, b) pitching moment control power, and c) aerodynamic efficiency vs α.

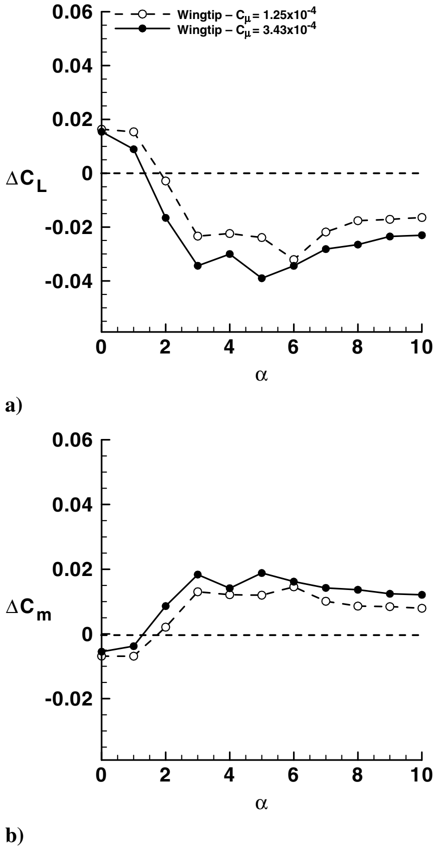

Fig. 9 Sinusoidal waveform excitation of only two synthetic jets at the wingtip: a) lift control power and b) pitching moment control power vs α.

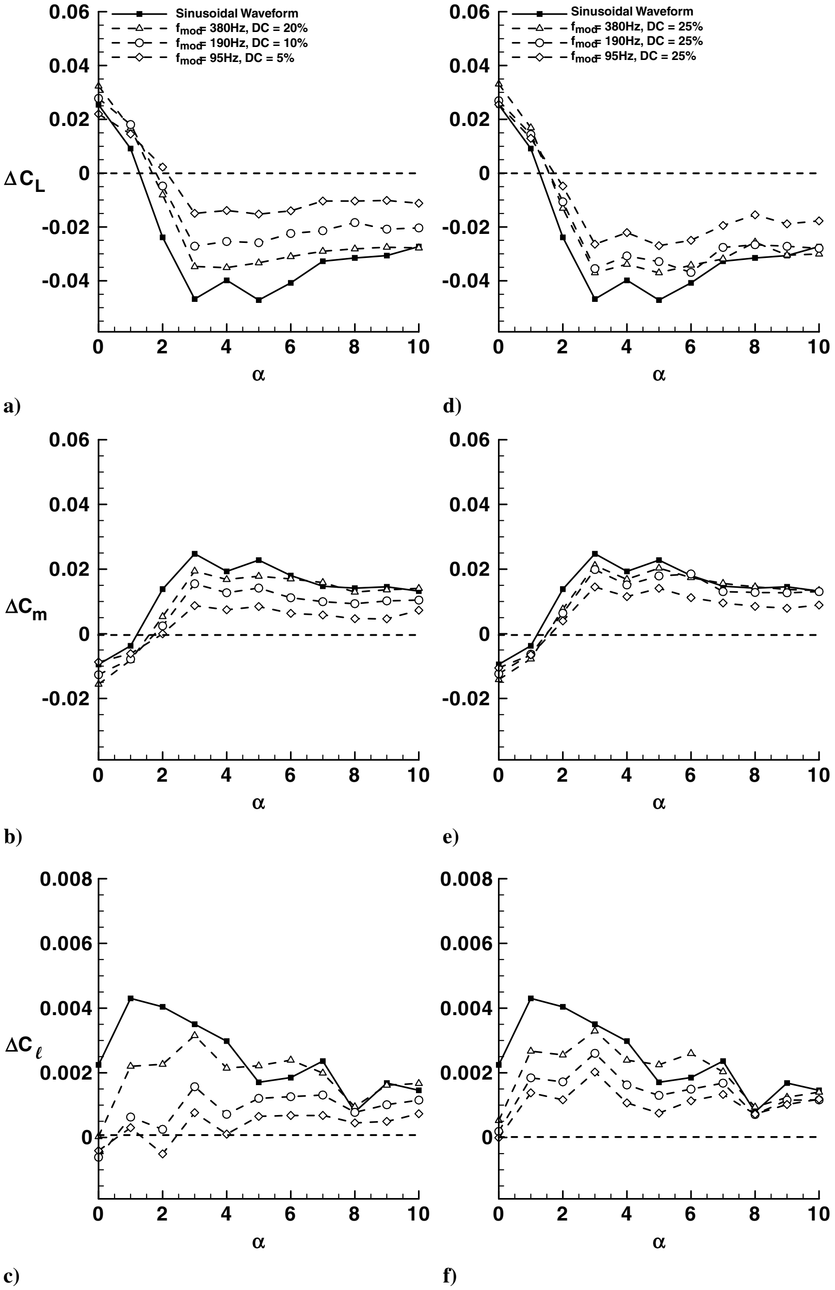

Fig. 10 Control power vs α for various frequency modulations: a, d) lift; b, e) pitching moment; and c, f) rolling moment; a–c) one cycle of the carrier frequency, and d–f) 25% duty cycle where $C_m = 5.14 \times 10^{-4}$ for (a–b, d–e), and $C_\mu = 2.57 \times 10^{-4}$ for (c, f).

negative value throughout the range of angles of attack tested and is relatively constant for $2 \leq \alpha \leq 8$ deg (Fig. 7b), as expected. As the elevons are deflected down, the pitching moment becomes more negative (nose down), whereas negative elevon deflection results in an increase in the pitching moment (i.e., less negative and positive for $\delta_e \geq 10$ deg, nose up). These plots demonstrate the conventional anticipated aerodynamic performance of a deltalike wing at low angles of attack, which correlate nicely with previous work done on the Stingray UAV (Parekh et al. [16]).

B. Global Measurements with Synthetic Jets

In previous work (Amitay et al. [14,15], Parekh et al. [16], and Washburn and Amitay [17]) the synthetic jet actuation was implemented at the leading edge. In the current experiments, the synthetic jets are located on the suction side (top surface) of the model, 6.5 mm normal to the leading edge (similar to the model tested by Farnsworth et al. [23]).

The following subsections discuss the effects of the actuation produced by three groups of synthetic jets. The first group includes activation of all 12 synthetic jets, the second group uses only six synthetic jets (SJ01, SJ03, and SJ04 on each wing, see Fig. 2), and the third group includes the synthetic jets near the wingtip (SJ05 and SJ06). For each group, data were collected for symmetric actuation (i.e., the synthetic jets on both sides of the wing were activated) to investigate the longitudinal control power (i.e., pitch control), and for asymmetrical actuation (only the starboard jets activated) to investigate the lateral control power (i.e., roll control). Note that the changes in the yaw moment (when control was applied) were within the resolution of the sting and thus are not presented.

1. *Effect of Momentum Coefficient*

The effect of the momentum coefficient on the aerodynamic performance of the Stingray UAV is presented here. The idea of incrementally adjusting the amplitude of the driving signal to the

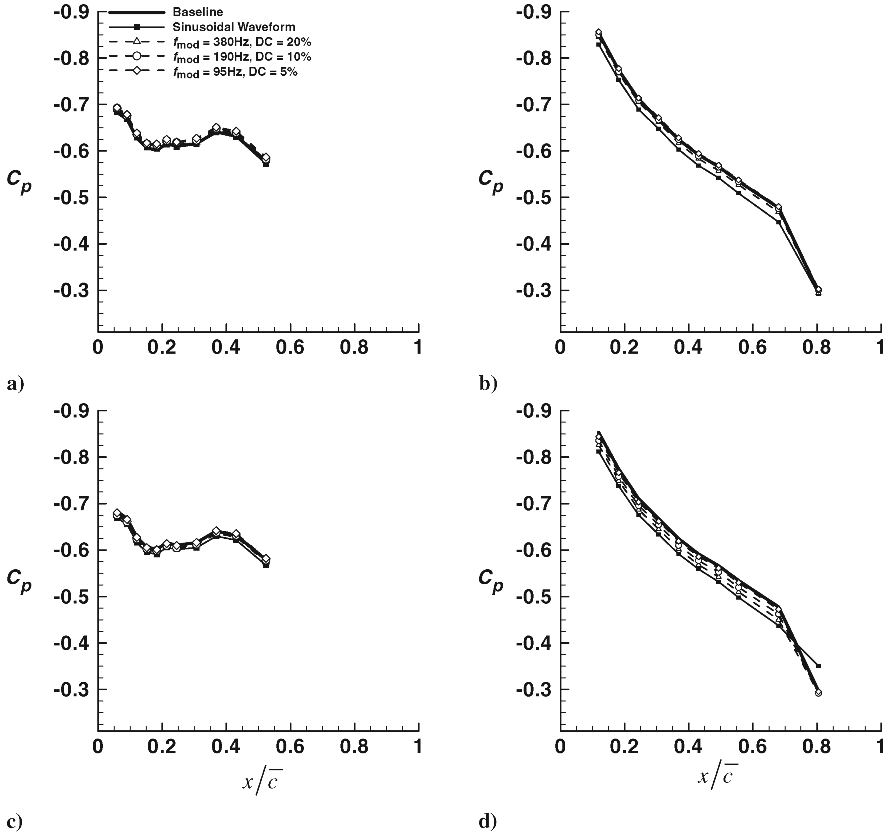

Fig. 11 **Pressure coefficient distributions for six synthetic jets: a, c) $C_\mu = 5.14 \times 10^{-4}$; and 12 synthetic jets: b, d) $C_\mu = 1.03 \times 10^{-3}$ at $y/b = 0.33$ for (a–b), and 0.66 (c–d) at $\alpha = 4\,\text{deg}$.**

actuators, or the activation of selected actuators, to obtain proportional output of control affect on the vehicle is a highly desirable trait for future development of closed-loop control models. Figures 8a and 8b present the change (with respect to the baseline) in the lift and pitch coefficients, respectively, at the range of angles of attack from 0 to 10 deg, whereas Fig. 8c presents the aerodynamic efficiency L/D. In these figures, four values of C_μ are used (1.87×10^{-4}, 3.75×10^{-4}, 5.14×10^{-4}, and 1.03×10^{-3}), where the first and third cases correspond to activation of six synthetic jets, and the second and fourth cases correspond to activation of all 12 synthetic jets.

Figure 8a presents the lift control power as a function of angle of attack, where the activation of the synthetic jets yields a noticeable change in the lift; namely, below $\alpha \approx 2\,\text{deg}$, the activation of the synthetic jets for any of the momentum coefficients produces an increase in the observed lift, whereas for higher angles of attack, the lift coefficient is reduced. However, for the pitching moment control power (Fig. 8b), the inverse of this trend is observed, where below $\alpha \approx 2\,\text{deg}$, actuation results in an increase in the nose-down moment, whereas for $\alpha > 2\,\text{deg}$, the actuation results in a reduction of the nose-down moment. The lift and the pitching moment display similar proportional effects where, as C_μ is changed, for either the 6 or 12 synthetic jets, the control effect is increased. Moreover, when comparing the cases where either 6 or 12 jets are activated, it is clear that activation of 12 jets at a lower C_μ results in a larger effect (compared with the six jets case), suggesting that the C_μ is not the only parameter governing the control effectiveness. The location of the actuation can, in some instances, have an even more profound effect on the surrounding flowfield; this will be further discussed throughout the paper. Note that the effect of using elevons is also included in Figs. 8a and 8b where all four elevons are deflected at -5 deg. The effect of the synthetic jets is comparable to the case were all four elevons are deflected at $\sim -2\,\text{deg}$, which is more than enough to trim the vehicle in pitch.

The effect of the synthetic jets on the aerodynamic efficiency C_L/C_D is presented in Fig. 8c as a function of angle of attack. When

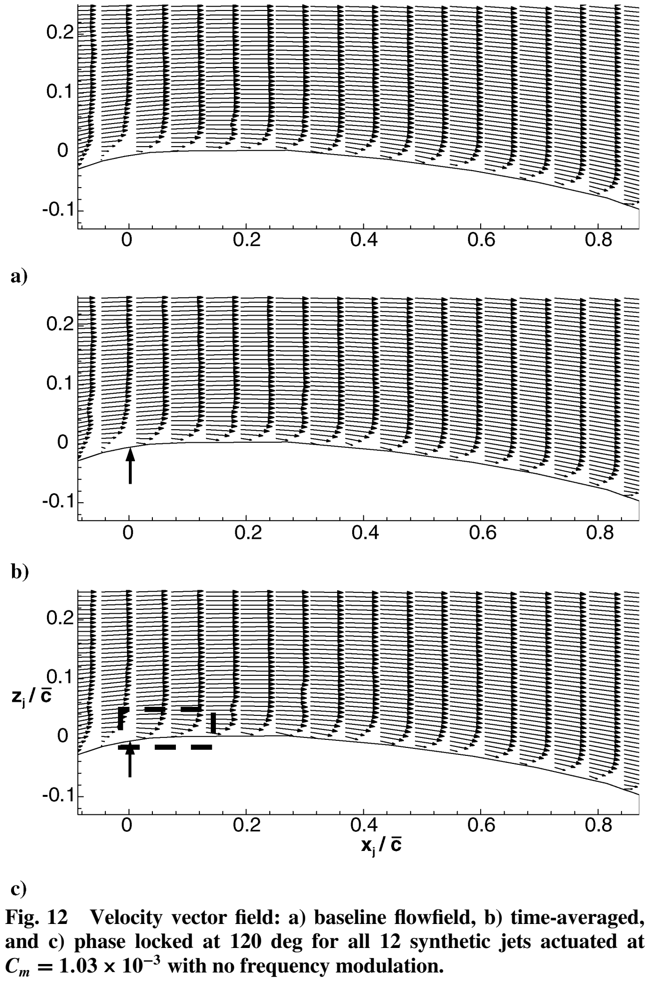

Fig. 12 **Velocity vector field: a) baseline flowfield, b) time-averaged, and c) phase locked at 120 deg for all 12 synthetic jets actuated at $C_m = 1.03 \times 10^{-3}$ with no frequency modulation.**

control is applied, the aerodynamic efficiency is similar to that of the baseline case, within the measurement uncertainty.

In Figs. 9a and 9b, longitudinal control is again observed through alteration of C_μ, where only the two synthetic jets that are located the closest to the wingtips are activated (SJ05 and SJ06 on each wing), and the momentum coefficient is varied from 1.25×10^{-4} to 3.43×10^{-4}. Through activating only these two jets at the wingtips, similar control effectiveness is observed when compared with the actuation of 6 and 12 jets across the wing (presented in Figs. 8a and 8b). This result further justifies the significance of the actuation location in the control data. Essentially, fluidic actuation on this configuration is more effective in producing longitudinal control near the wingtip (as displayed from comparing the six-actuators case to the two-actuators case). This result will be further discussed when analyzing the static pressure measurements and the PIV data in the later sections.

2. *Effect of Frequency Modulation*

Another way to obtain proportional control is to drive the synthetic jet with a pulse modulation waveform (see Fig. 4) instead of the continuous sinusoidal waveform. Using pulse modulation, the carrier frequency of the jet is held constant, thus the momentum coefficient *per carrier cycle* is held constant, but the power consumption of the jet is still altered as a function of the modulation frequency or the duty cycle.

In Fig. 10, the momentum coefficient (for one carrier frequency cycle) is held constant at 5.14×10^{-4} for the lift coefficient (Figs. 10a and 10d) and pitching moment (Figs. 10b and 10e) and 2.57×10^{-4} for the roll coefficient (Figs. 10c and 10f). However, when the modulation frequency is used (having a single cycle of the carrier frequency), the energy consumed by the synthetic jets for $f_{\text{mod}} = 95$, 190, and 380 Hz (with duty cycle of 5, 10, and 20%, respectively) is one-twentieth, one-tenth, and one-fifth the power compared to the continuous sinusoidal waveform case. Using modulation frequency yields proportional control in both longitudinal and lateral control.

Figures 10a–10c present the case where the duty cycle (for each modulation frequency) is selected such that a single cycle of the carrier frequency is produced, whereas Figs. 10d–10f show the case where the duty cycle is held constant at 25% for all three modulation frequencies. In both the single-cycle modulation and the 25% duty cycle cases, actuation results in proportional control; however, in the cases where the duty cycle and modulation frequency were coupled to produce one cycle per modulation period, the vehicle responds with a well-defined proportional effect. Proportional control is obtained for the longitudinal direction (pitching moment, Figs. 10b and 10e) as well as in the lateral direction (roll moment, Figs. 10c and 10f).

The preceding results show the global effect of the actuation (i.e., the effect on the moments and forces). To further explore the effect that the synthetic jets impose on the vehicle, the surface static pressure data were collected at two spanwise locations on the model and are presented in Fig. 11. Figures 11a and 11c display the pressure coefficient distribution at $y/b = 0.33$ and 0.66, respectively, for six synthetic jets being activated, whereas Figs. 11b and 11d present the pressure coefficient when 12 synthetic jets were activated. The effect of the synthetic jets on the static pressure coefficient is relatively subtle, <5% of the baseline value, but a noticeable proportional change in the static pressure coefficient is shown, especially for the pressure distribution closer to the wingtip (Figs. 11c and 11d).

These data display several key features: first, the alterations to the global forces and moments on the vehicle are also displayed through corresponding changes in the static pressure measurements, as would be expected. However, a more significant finding is associated with the difference in the two measurement locations. The pressure data support the previous supposition that the actuators display more control effectiveness toward the outboard portions of the wing (near

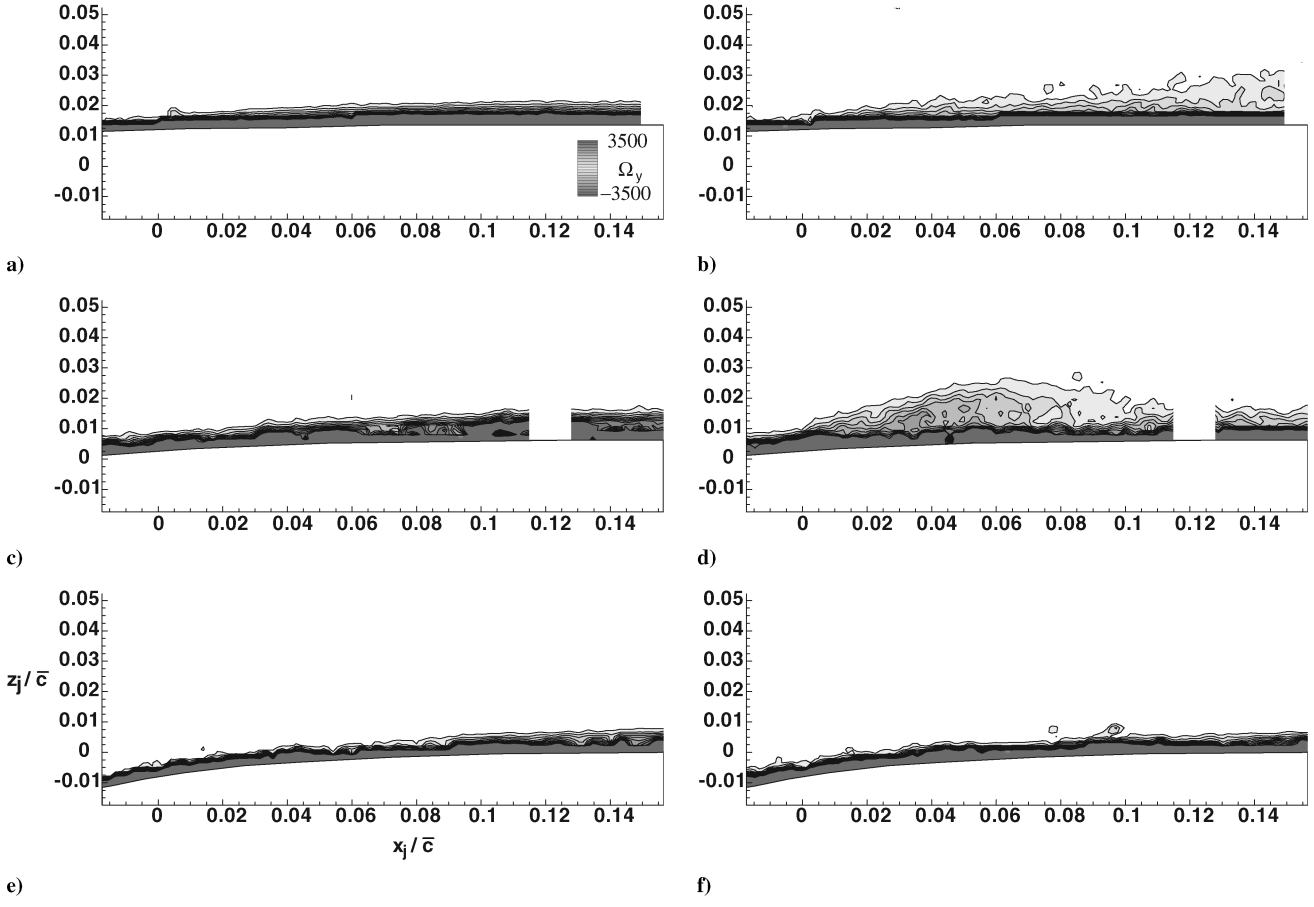

Fig. 13 Vorticity concentrations at SJ03 plane: a, c–d) baseline, and b, d, f) sinusoidal waveform actuation; a–b) inboard, c–d) centerline, and e–f) outboard planes for $C_\mu = 1.03 \times 10^{-3}$.

the wingtip). Clearly, from the pressure data, the inboard actuators produce only minute contributions to altering the flowfield. Also, when analyzing the outboard pressure data (Figs. 11c and 11d), it is worth mentioning that the activation of the actuators results in a slight increase to the static pressure (or reduction of negative pressure), which corresponds with the observed reduction in the global lift force on the model (Fig. 8a). Because the loss of lift is more significant toward the wingtip, a reduction in the nose-down pitching moment is measured (Fig. 8b), because the highly swept geometry places the wingtip aft of the moment reference center. The pressure results suggest an explanation for alterations to the global forces and moments, however, to explain physical physics of the pressure field alteration across the upper surface of the model, the velocity and vorticity fields were measured as discussed in the next section (Sec. III.C).

C. Particle Image Velocimetry Measurements with Synthetic Jets

To explain the effect of the synthetic jets on the global forces and moments, the flowfield over the Stingray was measured using PIV. Data at six two-dimensional streamwise measurement planes were acquired across the starboard wing of the Stingray UAV model (see Fig. 6). The data were acquired at three planes centered about SJ03a, b, and c ($y/b = 0.45, 0.48$, and 0.51) and three planes centered about SJ05a, b, and c ($y/b = 0.79, 0.82$, and 0.85) to understand the three-dimensionality of the flow within the local interaction domain of the synthetic jets. Also, in each of the following figures associated with PIV data, the flow is from left to right. Before conducting the PIV experiments, tuft flow visualizations were conducted on the Stingray vehicle verifying that, at $\alpha = 4$ deg (where the PIV measurements are taken), the flow is fully attached and predominately two-dimensional. Corresponding flow results were observed in the work by Ol [24] where a similar vehicle configuration, namely the 1303 UCAV, was tested in water through dye visualization and PIV measurements.

The following subsections focus on the local effects that the synthetic jets impose on the flowfield when all 12 synthetic jets are activated using a sinusoidal waveform with no modulation. A representative case of a low angle of attack of 4 deg is presented.

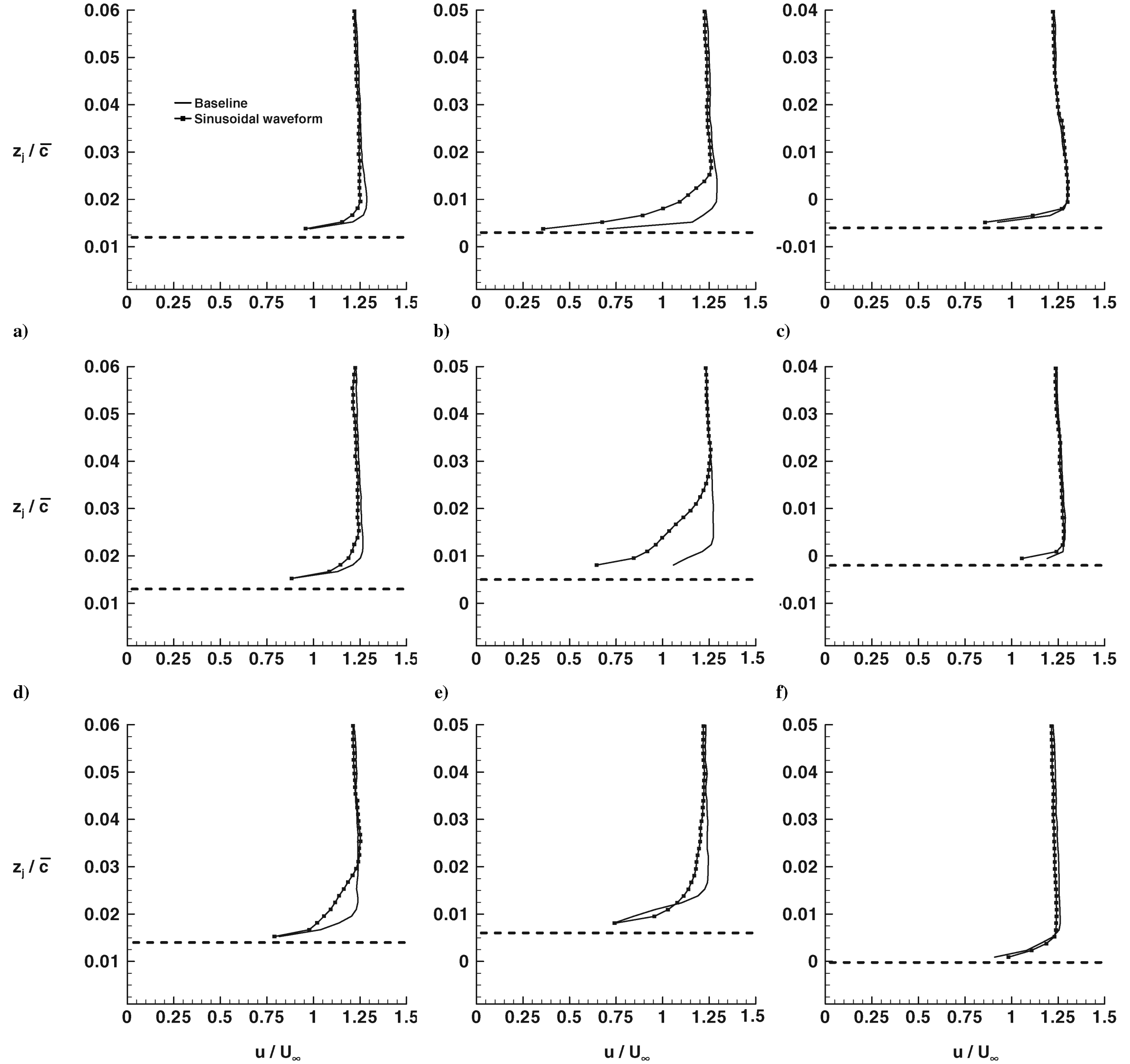

Fig. 14 Cross-stream distributions of the normalized streamwise velocity u/U_∞ for a–c) $x_j/c = 0.017$, d–f) 0.065, and g–i) 0.140 for the baseline and actuated cases; a, d, g) inboard, b, e, h) centerline, and c, f, i) outboard planes of SJ03 for $C_\mu = 1.03 \times 10^{-3}$.

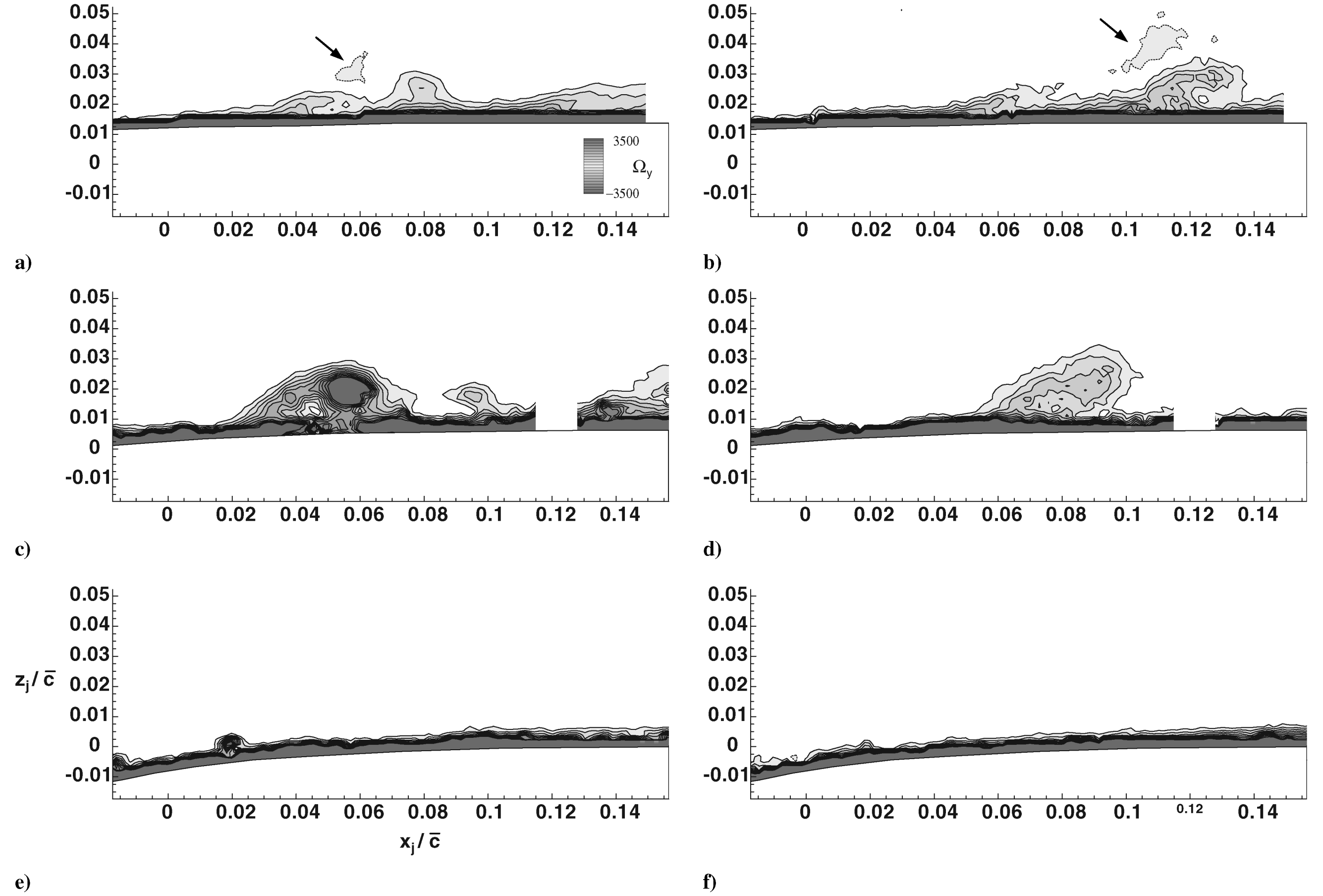

Fig. 15 Phase-locked vorticity concentrations at the SJ03 plane at a, c, e) 120 deg, and b, d, f) 240 deg; a–b) inboard, c–d) centerline, and e–f) outboard planes for $C_\mu = 1.03 \times 10^{-3}$.

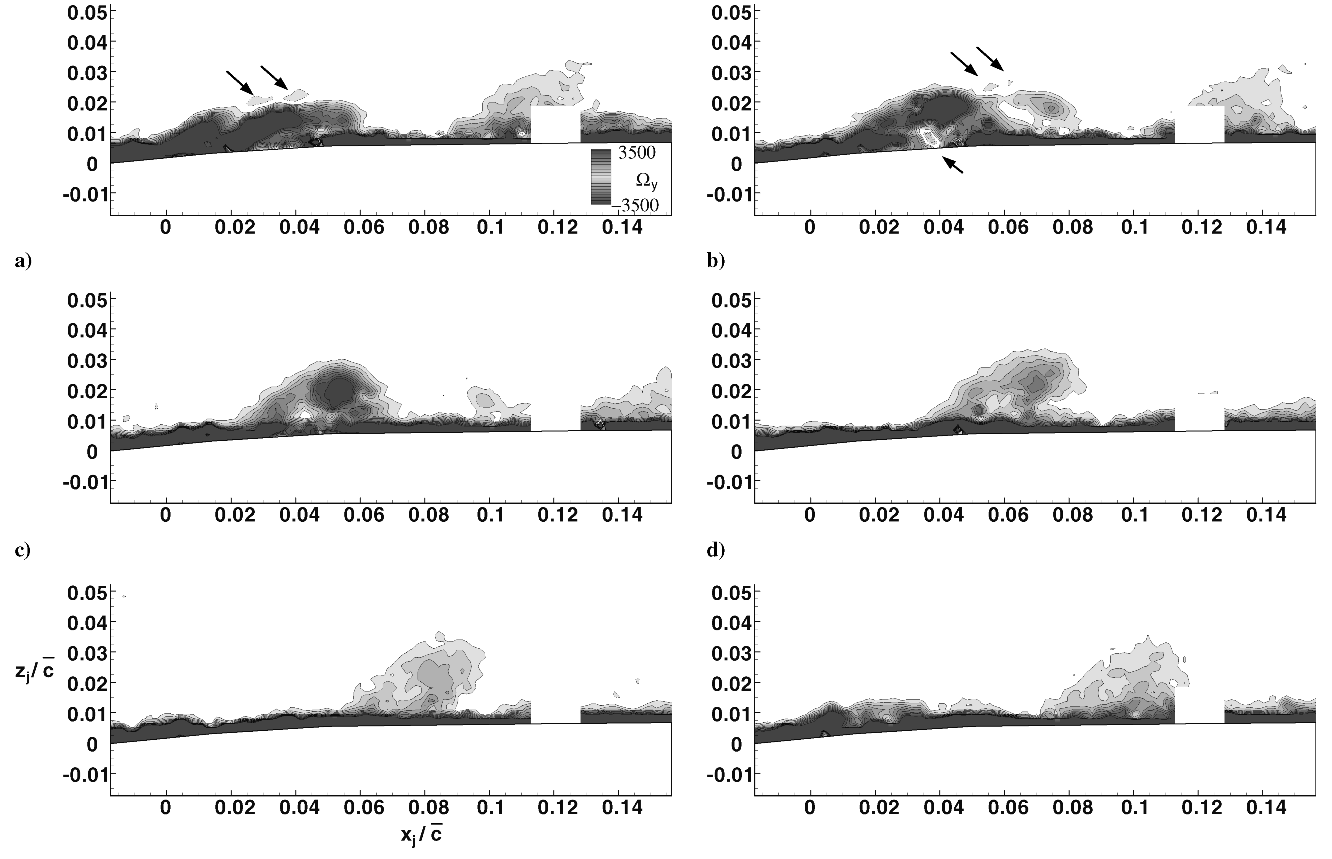

Fig. 16 Phase-locked vorticity concentrations at a) $\phi = 0$, b) 60, c) 120, d) 180, e) 240, and f) 300 deg at the centerline of SJ03 plane. $C_\mu = 1.03 \times 10^{-3}$.

1. Inboard Synthetic Jet Interactions (SJ03)

Figures 12a–12c display the velocity vector fields in the streamwise direction, along the centerline of the synthetic jet slot 03 (SJ03b, see location in Fig. 6). Figure 12a presents the velocity field of the baseline case (i.e., no actuation), whereas Figs. 12b and 12c correspond to the time-averaged and phase-locked forced cases, respectively. Note that the location of the synthetic jet in this plane is the origin of the coordinate system (x_j, $z_j = 0$, 0; marked with the arrow in Figs. 12b and 12c), and the phase-locked data were acquired at an angle of 120 deg (during the blowing portion of the cycle) in the synthetic jet carrier cycle. At this low angle of attack, the flow over the baseline model (Fig. 12a) is clearly attached to the surface, as expected. Furthermore, from these plots it looks like the synthetic jets induce no noticeable change on the global (time-averaged and phase-averaged) flowfields over the model. Therefore, to further explore the effect of the synthetic jets, a local interaction domain between the crossflow and the jets (marked by the dashed rectangle in Fig. 12c) has been investigated in detail.

Figures 13a–13f present the zoomed-in, time-averaged vorticity field for the baseline case (i.e., no actuation, Figs. 13a, 13c, and 13e) and the forced case (Figs. 13b, 13d, and 13f) at the three local measurement domains centered around synthetic jet orifice 03 (SJ03a, b, and c, respectively). The baseline flow exhibits an attached flow over the surface. When the synthetic jets are activated, there is a clear alteration of the vorticity field in the centerline case SJ03b (Fig. 13d) where the thickness of the vorticity layer, downstream of the synthetic jet slot, increases compared to the baseline case. Furthermore, by $x_j/\bar{c} = 0.12$, the thickness of the forced boundary layer is similar to that of the baseline case, suggesting that a quasi-steady-state "virtual bump" was formed downstream of the synthetic jet slot. When comparing the vorticity field to the off-centerline cases, it is apparent that no change (with respect to the baseline case) is visible at the outboard plane (SJ03c, Fig. 13f). However, at the inboard plane (SJ03a, Fig. 13b), the quasi-steady-state thickening of the boundary layer is apparent. At this location, the thickening does not begin until a distance of $x_j/\bar{c} = 0.1$ downstream of the orifice. This is probably due to the fact that the flow over the wing, at this location, has a spanwise inboard component due to the sweep of the wing, and thus the impulse from the synthetic jet advects both in the streamwise and spanwise directions.

To further understand the quasi-steady alterations of the boundary layer, Fig. 14 shows the cross-stream distributions of the normalized streamwise velocity component for three chordwise locations ($x_j/\bar{c} = 0.017$, 0.065, and 0.14; Figs. 14a–14c, Figs. 14d–14f, and Figs. 14g–14i, respectively) at each of the three spanwise measurement planes (SJ03a, b, and c; Figs. 14a, 14d, and 14g, Figs. 14b, 14e, and 14h, and Figs. 14c, 14f, and 14i, respectively). At locations SJ03a and b, the velocity gradient in the cross-stream z direction is noticeably reduced with the activation of the synthetic jets, causing a reduction in the shear stress at the wall. This is accompanied with thickening of the boundary layer that was observed and discussed previously (the effect is larger at the SJ03b plane). Moreover, at the SJ03a plane, the increase in the boundary-layer thickness (compared with the baseline case) becomes larger with downstream distance, whereas, at the SJ03b plane, the thickening of the boundary layer initially increases and then decreases toward the baseline value. Figures 14c, 14f, and 14i present the velocity profiles at SJ03c, where there is hardly any alteration of the boundary layer. The data presented in Figs. 14a–14i suggest that the effect of the synthetic jets is confined to a small region, in the vicinity of the jets; however, as was shown in Figs. 10–12, they induce a global modification on the vehicle (on the moments and forces). To estimate the error associated with the spatial resolution of the PIV, Fig. 14h is used as a test case. Here, the boundary-layer thickness for the baseline and actuated cases is approximately 2.5 and 5 mm, respectively, and the distance between vectors is 0.165 mm. This results in a spatial resolution $\Delta Z_j/\delta$ of 6.6 and 3.3%, respectively (corresponding to 8 and 16 vectors within the boundary layer).

The quasi-steady alteration to the flow, observed in the time-averaged data, is formed due to the fact that the actuation frequency is an order of magnitude larger than the characteristic frequency of the

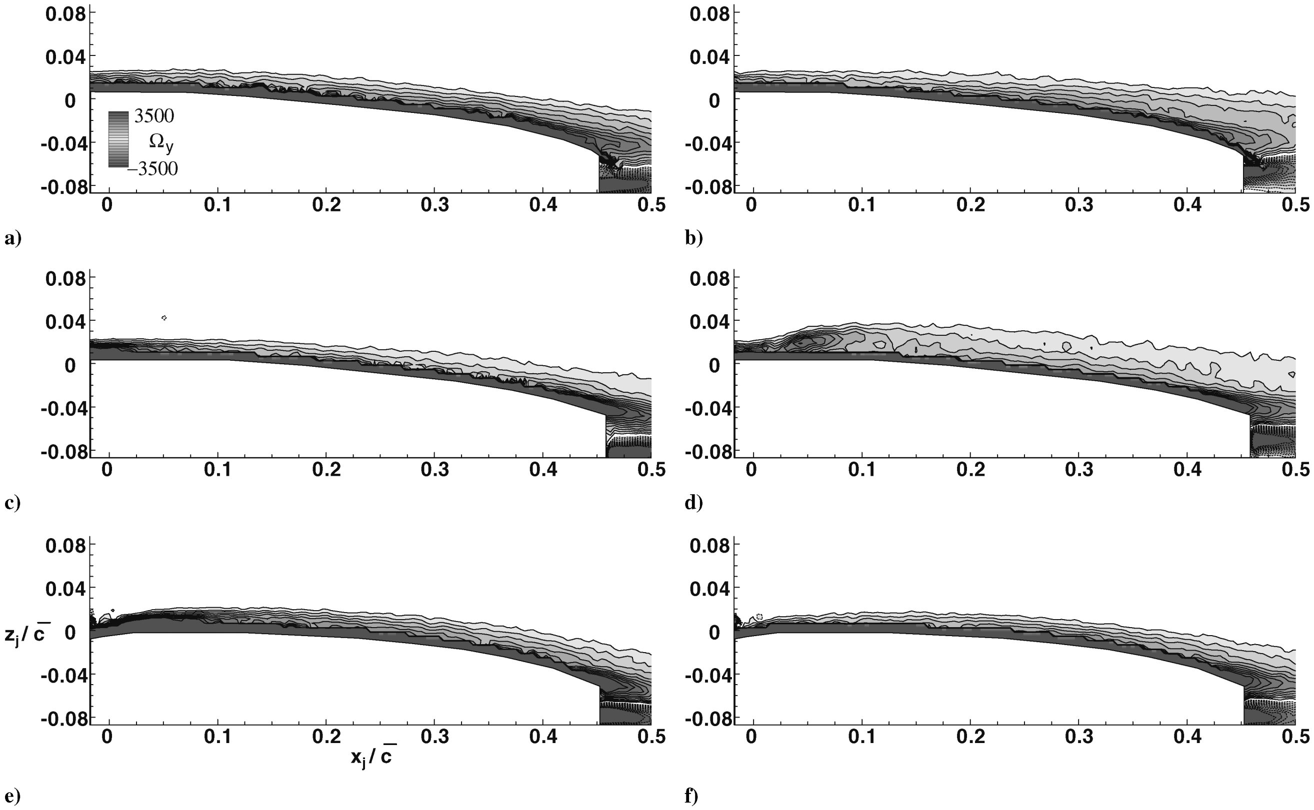

Fig. 17 Vorticity concentrations at SJ05 plane: a, c–d) baseline, and b, d, f) forced cases; a–b) inboard, c–d) centerline, and e–f) outboard planes for $C_\mu = 1.03 \times 10^{-3}$.

flow. To understand the formation of the quasi-steady region, data were also acquired phase locked to the carrier cycle of the synthetic jet actuator. First, data were acquired at two phases during the cycle for the three spanwise locations (SJ03a, b, and c). Figures 15a, 15c, and 15e present the phase-locked vorticity field at $\phi = 120\,\mathrm{deg}$, whereas Figs. 15b, 15d, and 15f display the vorticity fields for $\phi = 240\,\mathrm{deg}$. At $\phi = 120\,\mathrm{deg}$ on the centerline of the synthetic jet (SJ03b, Fig. 15c), a high concentration of positive vorticity is present in the flowfield just outside of the boundary layer downstream of the synthetic jet orifice ($x_j/\bar{c} = 0.06$), which is associated with the synthetic jet's previous cycle. Farther downstream, the reminiscence of the vorticity of the cycle before that is seen where the vorticity magnitude is smaller (compared with that at $x_j/\bar{c} = 0.06$). When $\phi = 240\,\mathrm{deg}$ (Fig. 15d), the vortical concentration is advected downstream and losses its strength. When analyzing the spatial development off of the centerline of the synthetic jet, similar positive vorticity concentrations are again observed at SJ03a (Figs. 15a and 15b); however, at SJ03c (Figs. 15e and 15f), vortical structures are not visible. This suggests that these vortical structures are advected downstream as well as inboard on the wing, displaying the complex three-dimensional nature of the interaction.

It is also worth noting that, in Figs. 15a and 15b, there appears a negative concentration of vorticity (marked by the arrows) in conjunction with the larger positive concentration. The production of these counter-rotating regions of vorticity is attributed to the basic nature of the synthetic jet. In the absence of a crossflow, the synthetic jet is known to induce counter-rotating vortex pairs (Glezer and Amitay [19]) due to its unique operation, thus when a crossflow is added, counter-rotating regions of vorticity are possible. The reason for the presence of unbalancing of the vorticity regions can be explained by the simple addition of the crossflow, which induces positive vorticity near the surface, thus enhancing the positive vorticity and weakening the negative vorticity produced by the synthetic jets.

The interaction of the synthetic jets with the crossflow is further explored by measuring the phase-locked (to the actuation cycle) flowfields at six different phases along the cycle of the synthetic jet. Figures 16a–16f present the phase-locked vorticity fields at $\phi = 0$,

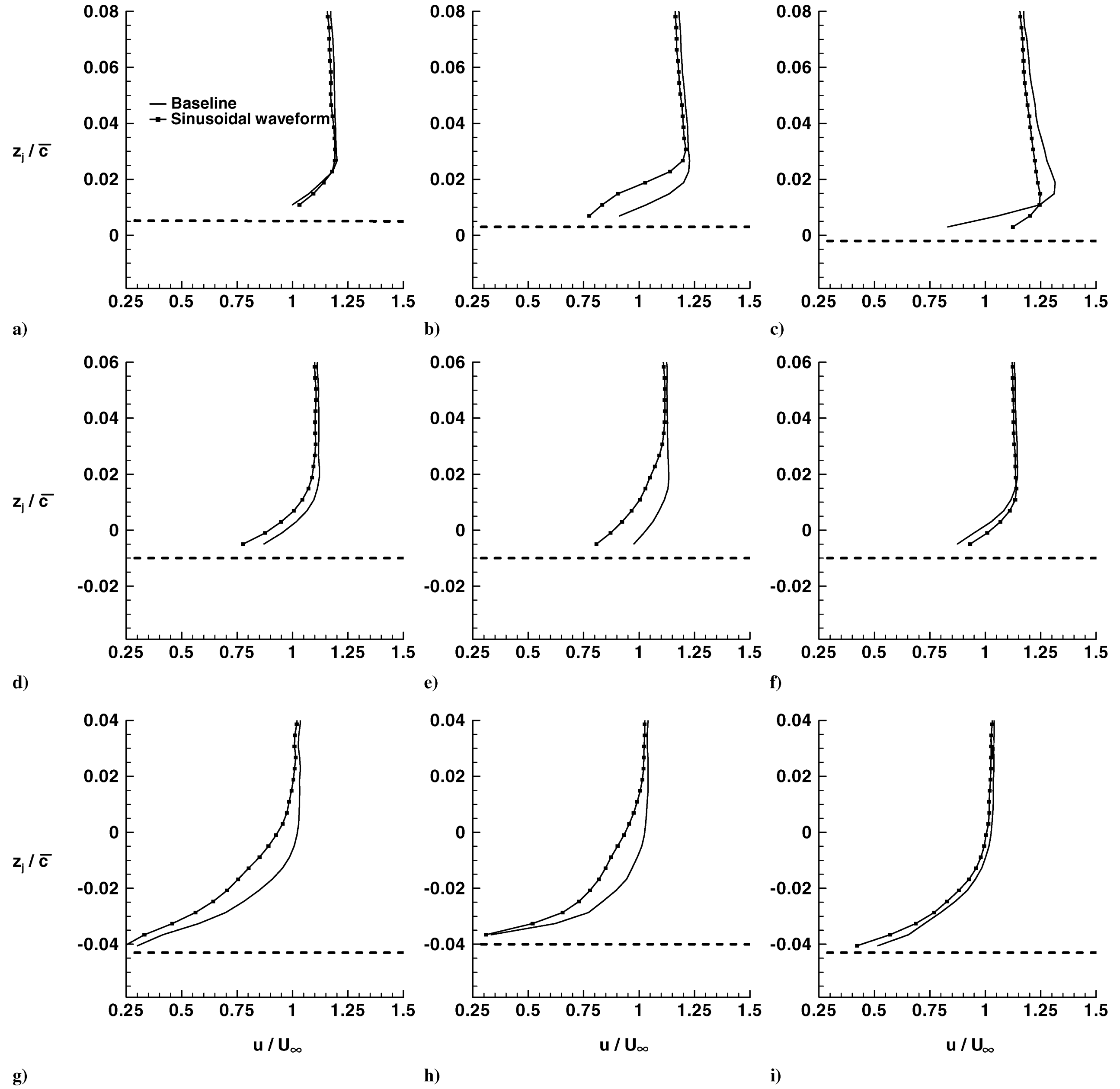

Fig. 18 Normalized velocity u/U_∞ vs z_j/c for a–c) $x_j/c = 0.043$, d–f) 0.26, and g–i) 0.43 for the baseline and forced cases; a, d, g) inboard; b, e, h) centerline; and c, f, i) outboard planes of SJ05 for $C_\mu = 1.03 \times 10^{-3}$.

60, 120, 180, 240, and 300 deg, respectively (note that phases at 0 and 180 deg correspond to the beginning of the blowing and suction portion of the cycle, respectively). Here, the formation and advection of vorticity concentration, associated with the vortex pair formed by the synthetic jet, is clearly visible as the vorticity concentrations travel downstream as the cycle progresses. At $\phi = 0$ deg (Fig. 16a), two vortical concentrations are present in the flowfield (at $x_j/\bar{c} \approx 0.04$ and 0.11), which are associated with the impulse of the previous synthetic jet cycles. These concentrations grow as they are advected downstream through $\phi = 120$ deg (Fig. 16c). At $\phi = 180$ deg (Fig. 16d), the structure associated with the previous cycle loses its coherence (and magnitude) as it detaches from the surface while advecting downstream. As the cycle continues ($\phi = 240$ deg, Fig. 16e), the structure is further diffused and a new structure is visible near the synthetic jet orifice, which is associated with the current impulse of the synthetic jet. Finally, at $\phi = 300$ deg (Fig. 16f), the impulse of the previous cycle continues to diminish, and the impulse of the current cycle is clearly visible immediately downstream of the synthetic jet slot. Note also the presence of small concentrations of negative vorticity, marked by the arrow, that are associated with the negative portion of the synthetic jet vortex pair. The entire growth and decay of the synthetic jet impulse occurs at a time scale that is an order of magnitude greater than the "time of flight" over the wing at this location ($t_{\mathrm{TOF}} = U_\infty / c_{\mathrm{local}}$). Moreover, within less than a nondimensional length of $\sim$14% of the mean chord, the vortical structures diminish and thus produce a quasi-steady virtual bump in the flowfield. Note that this small change contributes to the measurable alterations to the forces and moments for trim control, as previously discussed.

2. *Outboard Synthetic Jet Interactions (SJ05)*

The interaction of the synthetic jets with the crossflow was also examined near the wingtip (at the SJ05 plane, see location in Fig. 6). Figures 17a, 17c, and 17e and Figs. 17b, 17d, and 17f present the time-averaged vorticity fields for the baseline and forced cases, respectively, at SJ05a, b, and c planes (Figs. 17a and 17b, Figs. 17c and 17d, and Figs. 17e and 17f, respectively) across the full local chord of the outboard wing. Without flow control, there is a high concentration of positive vorticity near the surface due to the boundary layer, as expected. When the synthetic jets are activated, thickening of the boundary layer is observed, mainly at locations SJ05a and b (Figs. 17b and 17d, respectively), as was previously observed at the SJ03 plane. The largest thickening appears to be primarily on the centerline of the synthetic jet (location SJ05b, Fig. 17d), where the boundary-layer thickness is doubled. However, the effects are also noticeable off the centerline, especially on the inboard side of the synthetic jet (SJ05a, Fig. 17b). Note also the high vorticity concentration just downstream of the synthetic jet at $x_j/\bar{c} \approx 0.05$ (Fig. 17d).

Next, the effects of the synthetic jet on the boundary-layer development in planes SJ05a, b, and c are displayed in Figs. 18a–18i. Figures 18a–18c, Figs. 18d–18f, and Figs. 18g–18i correspond to the boundary layer profiles at $x_j/\bar{c} = 0.043$, 0.26, and 0.43, respectively, in locations SJ05a, b, and c (Figs. 18a, 18d, and 18g, Figs. 18b, 18e, and 18h, and Figs. 18c, 18f, and 18i, respectively). At $x_j/\bar{c} = 0.043$, the effect of the control is clearly visible in the centerline and outboard planes (Figs. 18b and 18c, respectively), whereas there is hardly any effect in the inboard plane (Fig. 18a). Farther downstream, at $x_j/\bar{c} = 0.26$, thickening of the boundary layer is obtained in the inboard plane (Fig. 18d), and a larger effect is observed in the centerline plane (Fig. 18e). However, the effect of the control on the boundary-layer profile in the outboard (Fig. 18f) diminishes. As the downstream distance increases, the effect of the synthetic jets becomes more pronounced in the inboard plane (Fig. 18g), whereas the alteration of the boundary layer along the centerline plane is smaller (Fig. 18h). Moreover, at this downstream location, the boundary layer along the outboard plane (Fig. 18i) is hardly affected by the activation of the synthetic jets. The results presented in Fig. 18 support the finding at the upstream location (at the SJ03 plane), where the effect of the synthetic jets is localized and is convected both downstream and inboard, as will also be discussed in Fig. 19.

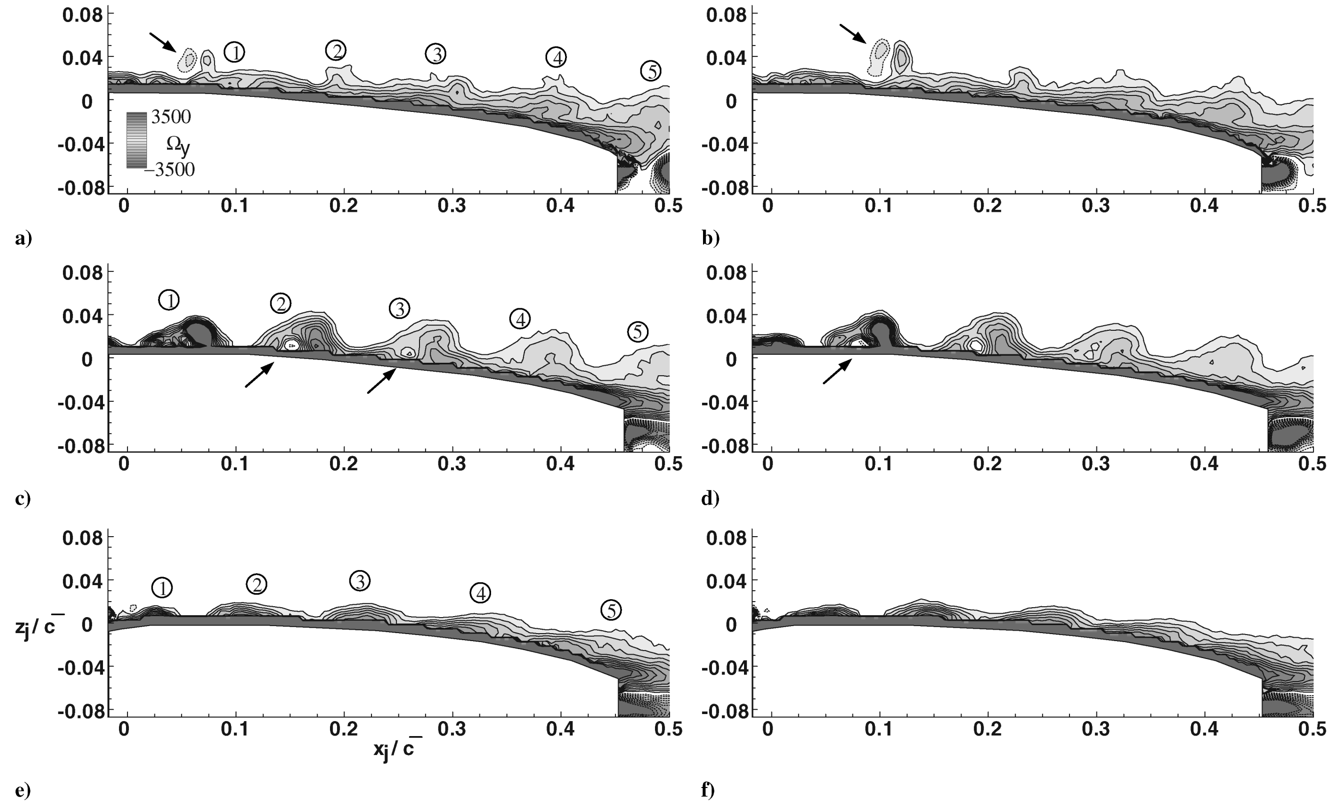

Fig. 19 Phase-locked vorticity concentrations at the SJ05 plane at a, c, e) 120 deg, and b, d, f) 240 deg; a–b) inboard, c–d) centerline, and e–f) outboard planes for $C_\mu = 1.03 \times 10^{-3}$.

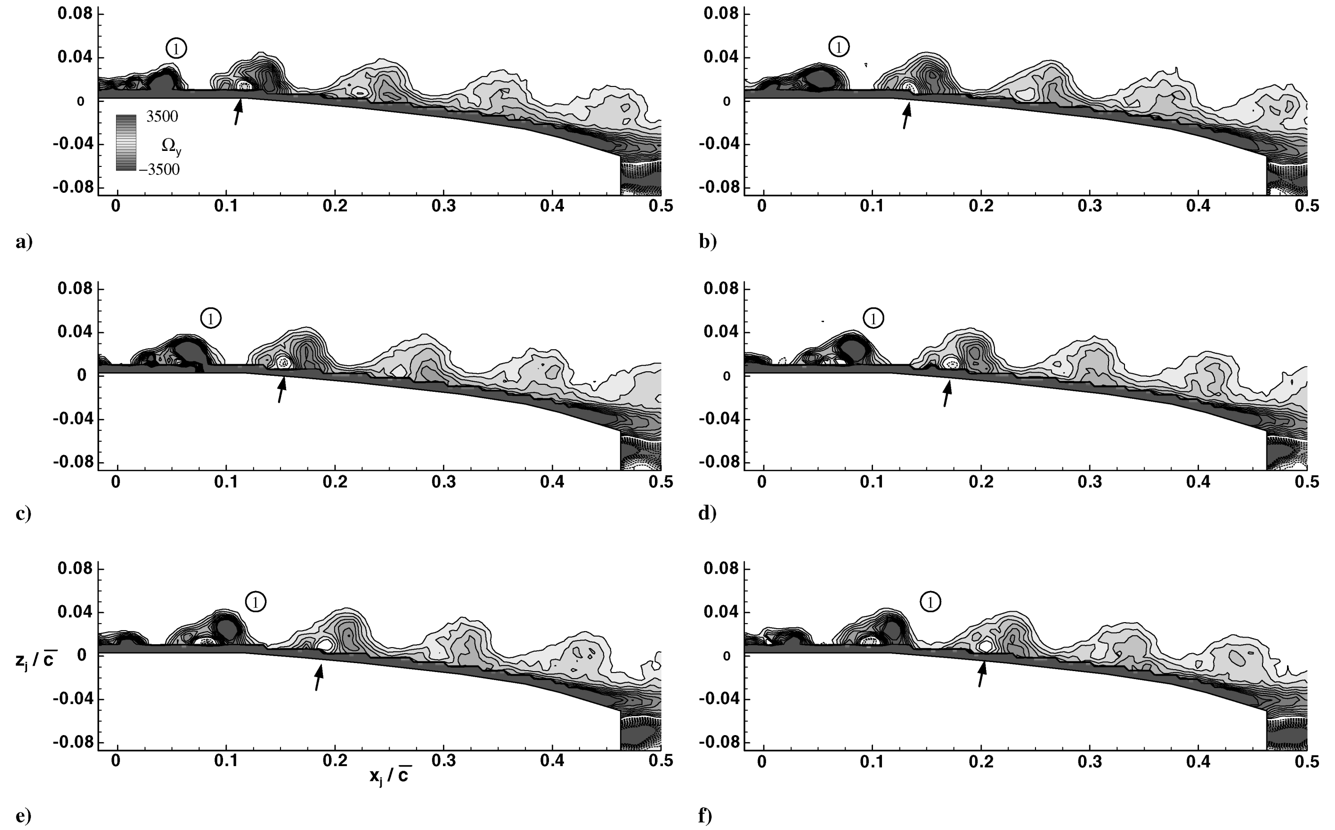

Fig. 20 **Phase-locked vorticity concentrations at a) $\phi = 0$, b) 60, c) 120, d) 180, e) 240, and f) 300 deg at the centerline of SJ05 plane. $C_\mu = 1.03 \times 10^{-3}$.**

To further explore the interaction domain, phase-locked data were acquired and are presented in Figs. 20a–20f, where the vorticity fields phase locked at $\phi = 120$ and 240 deg are displayed at SJ05a, b, and c measurement planes. As was shown in the SJ03 planes, the quasi-steady thickening of the boundary layer is caused by the high-frequency advection of vortical concentrations. Similar structures are observed in the SJ05 planes, as is shown in Figs. 19a–19f. The strength and coherence of these structures are the largest along the centerline plane, whereas off the centerline, they are weaker. Note the arrows on the figures that mark the negative vorticity concentrations, which is the negative portion of the synthetic jet's vortex pair. Moreover, the locations of the vortical structures (numbered) show their spanwise advection, as was also the case in the SJ03 planes.

Finally, the formation and advection of the vortical structures are presented in Figs. 20a–20f, at six equally spaced phases, via the phase-locked vorticity fields along the SJ05 centerline plane (SJ05b). From the phase-locked progression, coherent vortical concentrations are formed just downstream from the synthetic jet orifice, initially grow in size and advect with the cross-stream velocity (with diminishing strength), and are shed into the wake. The vorticity associated with the synthetic jet's previous cycle is marked with the number 1, as a representative vortical concentration. This shows the formation and advection of the coherent vorticity concentration during the synthetic jet cycle. (Note the presence of negative vorticity in Figs. 20e and 20f, representing the negative vorticity associated with the synthetic jet's impulse.)

By associating the PIV results with the previously discussed global forces and moments, as well as the static pressure measurements, a clear correspondence is observed. Namely, the same difference in effectiveness of the synthetic jets between the two spanwise locations is observed in the PIV results as was previously discussed in the force and pressure measurements. At each spanwise location, time-harmonic vortical structures are produced and advected downstream; however, the strength of these structures at the inboard location, SJ03, diminishes much faster than that of the outboard location, SJ05. As previously stated, because the actuation frequency is an order of magnitude larger than the characteristic frequency of the flow over the vehicle, the actuation results in a quasi-steady thickening of the boundary layer, which increases the static pressure on the upper surface of the wing, inducing a reduction in the local lift. Through the global alteration of the lift distribution across the wing, the global forces and moments can then be altered, providing control authority to the vehicle. Furthermore, through manipulation of the actuators' frequency and momentum coefficient, the advection frequency and strength of the vortical structures can thus be controlled, providing proportional control of the local time-averaged boundary-layer thickness as observed by the proportional changes to the global forces and moments.

IV. Conclusions

This paper presents an experimental investigation of a technique for control of the Stingray UAV in longitudinal (pitch) and lateral (roll) motions at low angles of attack using flow control via synthetic jets. The control effectiveness of the synthetic jets on the aerodynamic performance of the Stingray UAV was investigated in wind-tunnel experiments. Global flow measurements were conducted, where the moments and forces on the vehicle were measured using a six-component sting balance. Static pressure measurements on the upper (suction surface) were obtained at two spanwise locations, whereas a PIV system was used to quantify the flowfield over the model.

The synthetic jets were able to displace the local streamlines through the formation of a small quasi-steady interaction region on the suction surface of the Stingray UAV's wing. Detailed PIV measurements were performed, providing insight into the growth, propagation, and decay of the synthetic jets impulse and their interaction with the crossflow. Although the effect of the synthetic jets is localized, it is sufficient to induce global changes on the moments and forces to enable possible vehicle control. It was shown that the changes to the global moments and forces can be proportionally controlled by either changing the momentum coefficient or by driving the synthetic jets with a pulse modulation waveform. Using active flow control, proportional control of both the longitudinal and lateral directions was exhibited, leading the way for future development of closed-loop control models.

Acknowledgments

This project has been supported through partial support from Northrop Grumman Corporation and the U.S. Air Force Research Laboratory, as well as internal funding from Rensselaer Polytechnic Institute. The authors would like to thank Joshua Wood for his help in constructing the model and Steven London for his help in acquiring the particle image velocimetry data.

References

[1] Ho, C.-M., and Huerre, P., "Perturbed Free Shear Layers," *Annual Review of Fluid Mechanics*, Vol. 16, Jan. 1984, pp. 365–424. doi:10.1146/annurev.fl.16.010184.002053

[2] Oster, D., and Wygnanski, I. J., "Forced Mixing Layer Between Parallel Streams," *Journal of Fluid Mechanics*, Vol. 123, Oct. 1982, pp. 91–130. doi:10.1017/S0022112082002973

[3] Roberts, F. A., "Effects of Periodic Disturbances on Structure of Mixing in Turbulent Shear Layers and Wakes," Ph.D. Thesis California Inst. of Technology, Pasadena, CA, 1985.

[4] Seifert, A., Darabi, A., and Wygnanski, I., "Delay of Airfoil Stall by Periodic Excitation," *Journal of Aircraft*, Vol. 33, No. 4, 1996, pp. 691–698. doi:10.2514/3.47003

[5] Chatlynne, E., Rumigny, N., Amitay, M., and Glezer, A., "Virtual Aero-Shaping of a Clark-Y Airfoil Using Synthetic Jet Actuators," AIAA Paper 2001-0732, 2001.

[6] Amitay, M., Smith, D. R., Kibens, V., Parekh, D. E., and Glezer, A., "Aerodynamic Flow Control over an Unconventional Airfoil Using Synthetic Jet Actuators," *AIAA Journal*, Vol. 39, No. 3, 2001, pp. 361–370.

[7] Sheta, E. F., Siegel, J. M., Golos, F. N., and Harrand, V. J., "Twin-Tail Buffet Simulation Using a Multi-Disciplinary Computing Environment (MDICE)," *CEAS/AIAA/CASE/NASA Langley International Forum on Aeroelasticity and Structural Dynamics*, NASA CFD Research Paper, 1999.

[8] Mitchell, A. M., and Delery, J., "Research into Vortex Breakdown Control," *Progress in Aerospace Sciences*, Vol. 37, No. 4, 2001, pp. 385–418. doi:10.1016/S0376-0421(01)00010-0

[9] Gutmark, E., and Guillot, S., "Control of Vortex Breadown over Highly Swept Wings," *AIAA Journal*, Vol. 43, No. 9, 2005, pp. 2065–2069. doi:10.2514/1.11326

[10] Margalit, S., Greenblatt, D., Seifert, A., and Wygnanski, I., "Delta Wing Stall and Roll Control Using Segmented Piezoelectric Fluidic Actuators," *Journal of Aircraft*, Vol. 42, No. 3, 2005, pp. 698–709. doi:10.2514/1.6904

[11] Huang, A., Folk, C., Silva, C., Christensen, B., Chen, Y., Lee, G. B., Chen, M., Newbern, S., Jiang, F., Grosjean, C., Ho, C. M., and Tai, Y. C., "Application of MEMS Devices to Delta Wing Aircraft," AIAA Paper 2001-0124, 2001.

[12] Perkins, C. D., and Hazen, D., "Some Recent Advances in Boundary Layer and Circulation Control," *Fourth Anglo-American Aeronautical Conference*, Royal Aeronautical Society, London, 1953.

[13] Mandl, P., "Effect of Standing Vortex on Flow About Suction Aerofoils with Split Flaps," National Research Council of Canada, National Research Council of Canada Technical Rept. 234, 1959.

[14] Amitay, M., Washburn, A. E., Anders, S. G., Parekh, D. E., and Glezer, A., "Active Flow Control on the Stingray UAV: Transient Behavior," AIAA Paper 2003-4001, 2003.

[15] Amitay, M., Washburn, A. E., Anders, S. G., and Parekh, D. E., "Active Flow Control on the Stingray UAV: Transient Behavior," *AIAA Journal*, Vol. 42, No. 11, 2004, pp. 2205–2215. doi:10.2514/1.5697

[16] Parekh, D. E., Williams, S., Amitay, M., Glezer, A., Washburn, A. E., Gregory, I., and Scott, R. C., "Synthetic Jet Aerodynamic Control on a Full-Scale UAV," AIAA Paper 2003-4002, 2003.

[17] Washburn, A. E., and Amitay, M., "Active Flow Control on the Stingray UAV: Physical Mechanisms," AIAA Paper 2004-0745, 2004.

[18] Chen, F. J., and Beeler, G. B., "Virtual Shaping of a NACA-0015 Airfoil Using Synthetic Jet Actuator," AIAA Paper 2002-3273, 2002.

[19] Glezer, A., and Amitay, M., "Synthetic Jets," *Annual Review of Fluid Mechanics*, Vol. 34, Jan. 2002, pp. 503–529. doi:10.1146/annurev.fluid.34.090501.094913

[20] Amitay, M., and Cannelle, F., "Evolution of Finite Span Synthetic Jets," *Physics of Fluids*, Vol. 18, No. 5, May 2006, p. 054101. doi:10.1063/1.2196093

[21] Cannelle, F., and Amitay, M., "Synthetic Jets: Spatial Evolution and Transitory Behavior," AIAA Paper 2005-0102, 2005.

[22] Amitay, M., and Glezer, A., "Role of Actuation Frequency in Controlled Flow Reattachment over a Stalled Airfoil," *AIAA Journal*, Vol. 40, No. 2, Feb. 2002, pp. 209–216.

[23] Farnsworth, J., Cannelle, F., Ciuryla, M., and Amitay, A., "Control of the Stingray UAV at Low Angles of Attack," AIAA Paper 2007-321, 2007.

[24] Ol, M., "Water Tunnel Velocimetry Results for the 1303 UCAV Configuration," AIAA Paper 2006-2990, 2006.

F. Coton
Associate Editor